Available online at www.sciencedirect.com
SCIENCE DIRECT®
Journal of Nuclear Materials 322 (2003) 138–151
journal of nuclear materials
www.elsevier.com/locate/jnucmat

Effect of quenching rate on the β-to-α phase transformation structure in zirconium alloy

A.R. Massih [a,b,*], T. Andersson [c], P. Witt [c], M. Dahlbäck [d], M. Limbäck [d]

[a] *Quantum Technologies AB, Uppsala Science Park, Uppsala SE-75183, Sweden*
[b] *Malmö University, SE-205 06 Malmö, Sweden*
[c] *Sandvik Materials Technology, SE-811 81 Sandviken, Sweden*
[d] *Westinghouse, SE-721 63 Västerås, Sweden*

Received 13 March 2003; accepted 25 June 2003

Abstract

Microstructures of low-tin Zircaloy-2 specimens subjected to quenching from β to α phase have been studied using optical and scanning electron microscopy (SEM). The specimens were quenched at different cooling rates ranging from 3 to 83 K s^{-1}. Optical microscopy (OM) provided data on the α phase plate width which is correlated to the cooling rate. All the obtained structures after quenching indicate basket-weave morphology. In addition, OM furnished information on β phase grain size which is correlated to the holding time in β phase prior to quenching. SEM was used to characterise the second phase particles in regard to size distribution and mean size in two of the specimens quenched at the rates of 58 and 6.6 K s^{-1}. One of the specimens was annealed in the α phase after β-quenching, upon which particle sizes were measured. Physical-based models are used to evaluate and explain the microstructural properties observed in this experiment.

1. Introduction

Many technologically important properties of zirconium alloys, such as their mechanical strength and toughness, creep and corrosion resistance are essentially controlled by the presence of precipitated particles of a second phase and the morphology of the microstructure. This commonly results from the decomposition of the body-centred cubic (bcc) β phase to the hexagonal closed-pack (hcp) α phase and the intermetallic χ phase with their overlapping temperatures. For example, in Zircaloy-2 (Zr–1.3Sn–0.19Fe–0.lCr–0.06Ni by wt%) the temperature ranges are β above 1250 K, α + β between 1150 and 1250 K, α + β + χ between 1080 and 1150 K and α + χ below 1080 K [1]. In Zircaloy-2 the intermetallic compounds are formed by diffusion of the alloying elements iron, chromium and nickel from the base Zr matrix. The χ phase intermetallic, a generic label for second phase precipitated particles (SPP), together with the impurities present in Zircaloy have a strong influence on the kinetics of the phase transformation. In Zircaloy and other zirconium-base alloys the alloying elements determine the coexistence region of the α and β phases. For example, tin and oxygen (around 1200 ppm) stabilise the α phase, expanding the α region of the phase diagram at higher temperatures, while iron and chromium maintain the β phase stable at temperatures lower than for pure zirconium [1]. In particular, iron, chromium and nickel are considered as β-eutectoids, because in their phase diagrams, these elements have an eutectoid decomposition in β phase [2].

The β to α phase transformation in Zircaloy commonly yields to a so-called Widmanstätten microstructure [3]. This microstructure can manifest itself into two types of morphology referred to as the basket-weave structure and the parallel-plate structure, respectively, as noted by Ökvist and Källström in Zircaloy-2 [4]. The basket-weave structure appears as relatively short plates

* Corresponding author. Fax: +46-1850 9890.
E-mail address: alma@quantumtech.se (A.R. Massih).

0022-3115/$ - see front matter © 2003 Elsevier B.V. All rights reserved.
doi:10.1016/S0022-3115(03)00323-4

intersecting each other within the parent β-grains. Its formation is associated with an abundance of nucleation sites for the α phase, present in the β phase, during cooling from the β phase temperature region. The parallel-plate structure is composed of long plates and grows from the parent β-grain boundaries. Carbon, silicon and phosphorus are examples of low solubility elements (impurities) which act as nucleation sites for the basket-weave structure in Zircaloy [4,5]. Other impurities such as chlorine, magnesium, calcium, sodium, potassium may be present in Zircaloy products. These impurities are referred to as inclusions or stringers. Charquet and Alheritiere [6] by examining several hundred industrial Zircaloy-2 and Zircaloy-4 billets (170 mm diameter), that were water quenched from β phase and contained 50–120 ppm carbon, 20–50 ppm silicon and 5–10 ppm phosphorous, found that (i) materials containing stringers form basket-weave structure; (ii) materials free of stringers form parallel-plate structure.

The effect of cooling rate on Zircaloy-4 (Zr–1.5Sn–0.2Fe–0.lCr by wt%) microstructure on $\beta \rightarrow \alpha$ transformation was studied by Holt [7,8]. Holt performed a range of cooling rates: 2, 11, 65, 200 and 2000 $K\,s^{-1}$ starting from 1123 K. Holt found that by increasing the cooling rate from 2 to 200 $K\,s^{-1}$ finer Widmanstätten plates are produced, while cooling at 2000 $K\,s^{-1}$ produced quenched martensitic structure. As has been noted by Charquet and Alheritiere [6], in Zircaloy for cooling rates faster than 1000 $K\,s^{-1}$ the martensite structure is observed, while for very slow cooling rates $\leqslant 0.5\ K\,s^{-1}$ the needle-shaped structure is no longer seen. Basket-weave and parallel-plate structures are observed between these two cooling rate limits.

Woo and Tangri [9] studied the effects of oxygen content and cooling rate on the microstructure of β-quenched Zircaloy-4. They examined Zircaloy-4 specimens that contained oxygen concentrations in the range 0.13–0.91 wt% and were subjected to cooling rates in the range 90–2000 $K\,s^{-1}$. They found that in the cooling rate of interest, 90 $K\,s^{-1}$, as oxygen concentration was increased from 0.13 wt%, the microstructure tended toward parallel-plate morphology. This effect took place in the following order: basket-weave-$\alpha \rightarrow$ parallel-plate-$\alpha \rightarrow$ lenticular-α.

Here we report the results of an experiment made to investigate the influence of cooling rate on microstructure of low-tin Zircaloy-2 cylindrical specimens quenched from high-temperature β phase to room temperature (RT), 323 and 373 K. The cooling rates employed ranged between 3 and 83 $K\,s^{-1}$. Using optical microscope (OM) we have measured β-grain size and α plate width for the specimens that had undergone different cooling rates. In addition, utilising scanning electron microscopy (SEM) we have determined the SPP size for two of the trials with distinct cooling rates (58 and 6.6 $K\,s^{-1}$). We also present our analyses of the experimental data, i.e. the SPP nucleation, growth and coarsening on β-quenching and -annealing. In addition, we discuss the dependence of the α plate width on cooling rate using the classical theory of domain growth.

2. Experimental

2.1. Material

The material chosen was a zirconium alloy with l.lSn–0.19Fe–0.lCr–0.06Ni by wt% in form of a solid billet with 100 mm diameter. In this paper the material is

Table 1
Chemical composition of zirconium alloy[a] (by weight)

Elements	End 1	End 2
Sn (%)	1.10	1.09
Fe (%)	0.195	0.190
Cr (%)	0.103	0.101
Ni (%)	0.061	0.060
O (ppm)	1200	1200
Si (ppm)	90	90
P (ppm)	<40	<40

[a] Low-tin Zircaloy-2.

Table 2
Cooling rates obtained from the tests on Zircaloy-2 specimens

Trial no.	T_q (K)	Cooling medium	Cooling rate ($K\,s^{-1}$)		
			T_q–1073 K, 5 mm depth	1273–1023 K, 5-mm depth	1273–1023 K, 20-mm depth
1	1273	Water RT	50	58	35
2	1323	Water RT	42	78	39
3	1323	Water RT	42	63	37
4	1323	Water 323 K	23	26	22
5	1323	Water 373 K	8	6.6	6.3
6	1323	Air RT	3.5	3	3
7	1373	Water RT	50	83	34
8	1473	Water RT	57	83	42
9	1303	Water RT		74	33

referred to as low-tin Zircaloy-2, although the Sn content is only slightly below the ASTM range [10]. The chemical analysis from the two ends of billet are given in Table 1. The billet was machined to 40 mm in diameter from which cylindrical pins with 60 mm length were produced by cutting.

2.2. Quenching

In order to investigate the effect of temperature and cooling rate on the microstructure, a number of cooling tests was performed at Sandvik laboratories in Sandviken, Sweden. Each cylinder was pierced at one end with holes at the centre and at 5 mm from the outer surface, respectively. Both holes were pierced half way through the cylinder in which thermocouples were placed for temperature measurements during heat up and cooling. In the tests the cylindrical samples were subjected to quenching from different temperatures in the range 1273–1473 K to RT in water and from 1323 K to water temperatures of 323 and 373 K. One sample was cooled to ambient RT in air. The samples were heat treated in a laboratory furnace and then were quenched in a 10 l tank containing 5 l of water. The water quenching was performed by plunging the cylinders in the water tank subjected to vigorous stirring. The cooling rates were

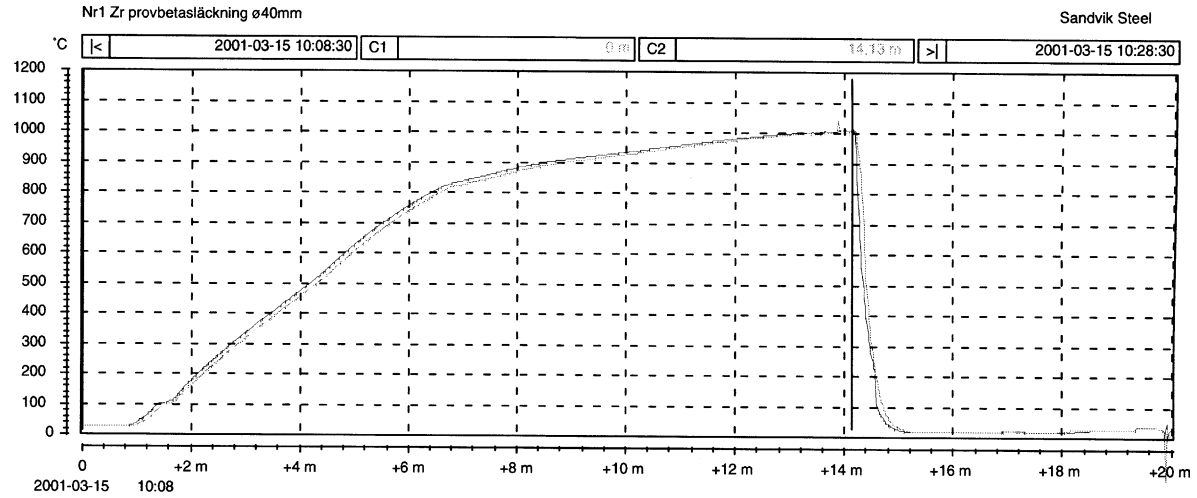

(a) Trial 1

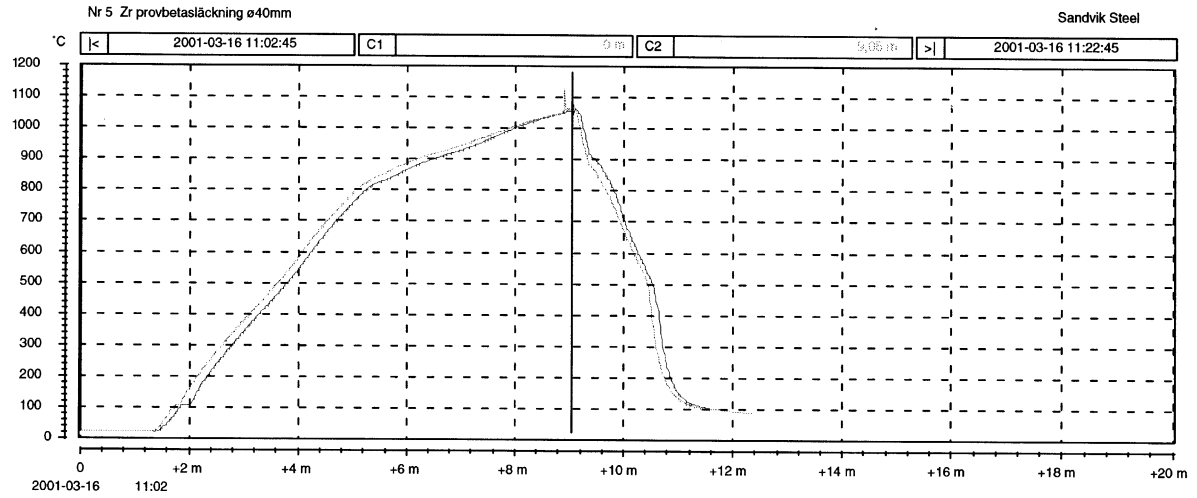

(b) Trial 5

Fig. 1. Temperature (°C) vs. time (min) directly recorded from thermocouples located at lateral depths of 5 and 15 mm, during heat-up and cool-down of Zircaloy-2 specimens β-quenched in water: (a) trial 1 specimen quenched from 1000 °C to room temperature, (b) trial 5 specimen quenched from 1050 to 100 °C.

estimated from the temperature history recordings. The cooling rates were determined from the quenching temperature T_q to 1073 K or in the interval 1273–1023 K. In Table 2 the results obtained from these tests are tabulated. We should mention that the samples experienced different temperature histories during the simulated heat treatments. For example, the hold-time in β phase for the trial 1 was roughly 1 min, while for the trial 3 it was about 12 min. Temperature histories for two of the trials (1 and 5) are shown in Fig. 1.

2.3. Metallography

Specimens were taken from each of the β-quenched cylinder for metallographic analysis. The specimens were cut out from the middle of each cylinder near the locations of thermocouples, in the radial depths of 5 and 15 mm, and then were examined by OM and SEM. The OM examination included characterisation of the morphology of the α phase structure, α-lamella width measurements and measurements of the prior β phase grain size. Even the presence of zirconium silicides was scrutinised. For two of the trials, trials 1 and 5 listed in Table 2, SPP were examined by SEM on specimens taken from radial depths of 5 and 15 mm. Also for trial 1, subsequent to β-quenching, the aforementioned parameters were studied after annealing the specimen at 973 K for 1 h.

2.4. Results

The morphologies of all the tested specimens indicated the basket-weave α phase structure. As a whole, higher cooling rates resulted in finer α-lamellae, whereas lower cooling rates produced coarser α-lamellae. Figs. 2 and 3 illustrate the features of the microstructures for specimens taken from trials 1 and 5 (Table 2), respectively. Lamella width data vs. cooling rate are plotted in Fig. 4. Prior β phase grain size vs. hold-time in β phase

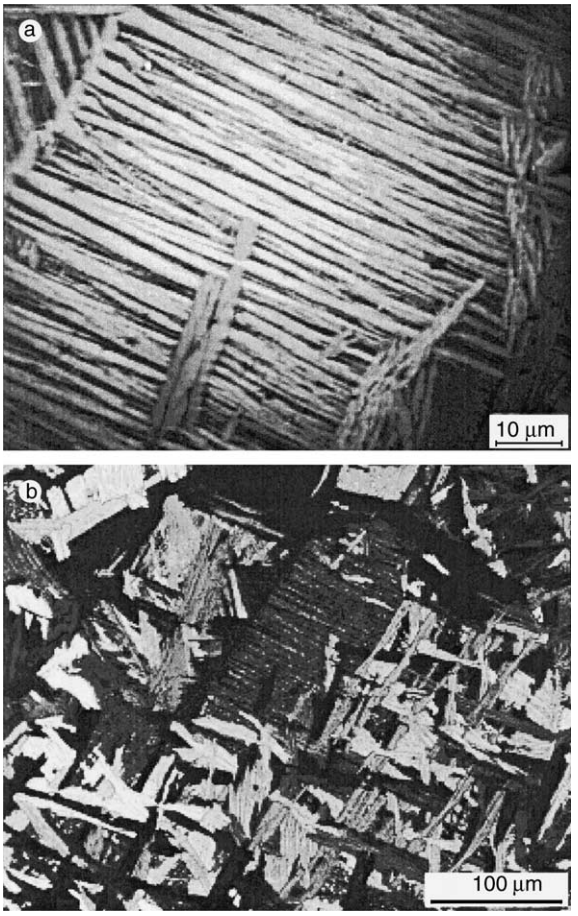

Fig. 2. Microstructure after β-quenching of trial 1 specimen (1273 K/water at room temperature), 5 mm from surface: 75 mm width.

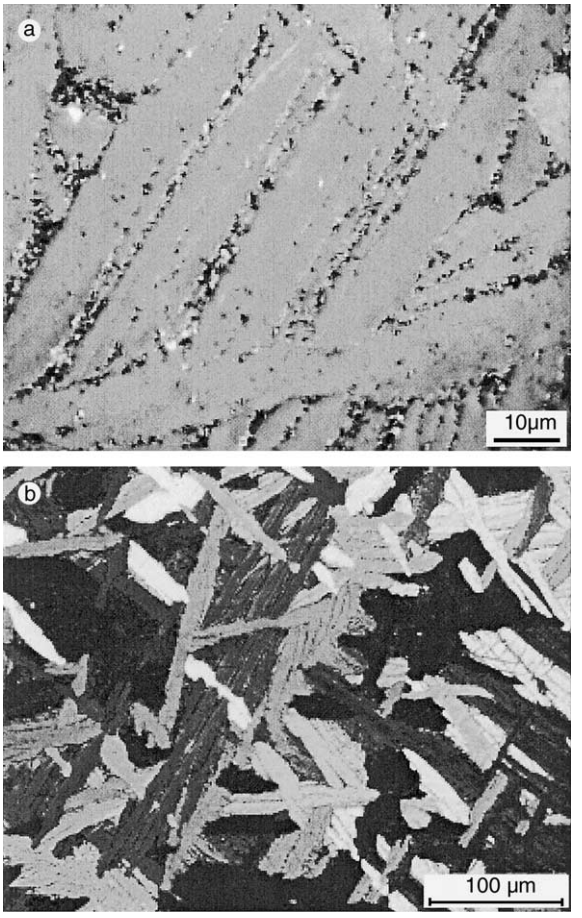

Fig. 3. Microstructure after β-quenching of trial 5 specimen (1323 K/water at 373 K), 5 mm from surface: 75 mm width.

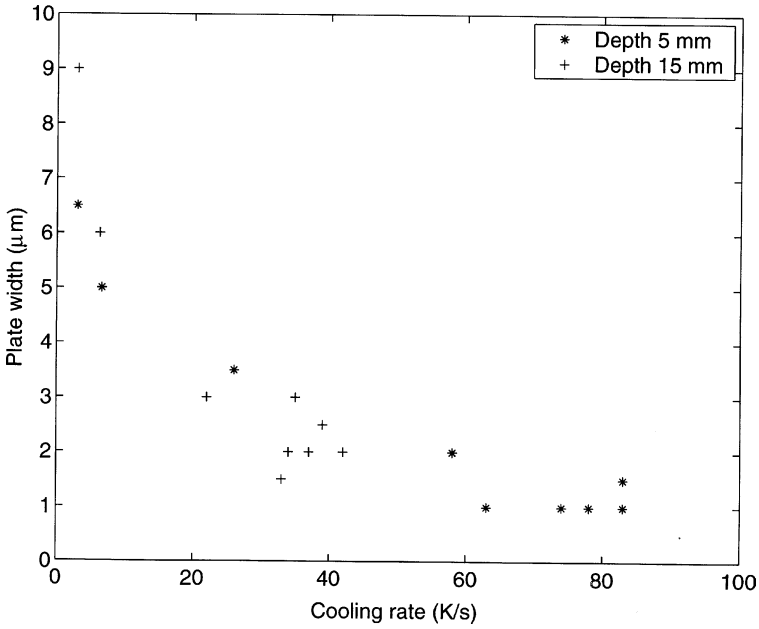

Fig. 4. Optical microscopy measurements of α-lamella thickness after β-quenching of specimens at different cooling rates.

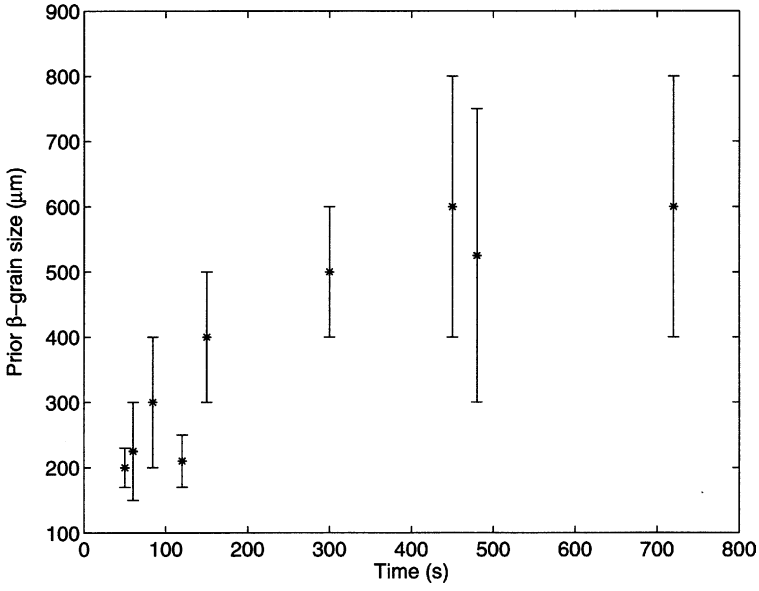

Fig. 5. Optical microscopy measurements of prior β phase grain size, at a lateral depth of 5 mm in the specimens. The time is measured from temperature history plots from 1273 K to the quenching temperatures T_q listed in Table 2.

(measured from 1273 K up to the quenching temperatures T_q, Table 2) are depicted in Fig. 5. We should note that there exists a large spread in β phase grain size and we have only determined their maxima and minima. The asterisks shown in Fig. 5 are the mean values of these extrema.

The results of SEM examinations for SPP are presented in Fig. 6 for trials 1 and 5. Their corresponding size distributions are shown in Fig. 7. The average SPP sizes for these specimens are collected in Table 3. The table also includes the results for trial 1 after annealing at 973 K h^{-1}.

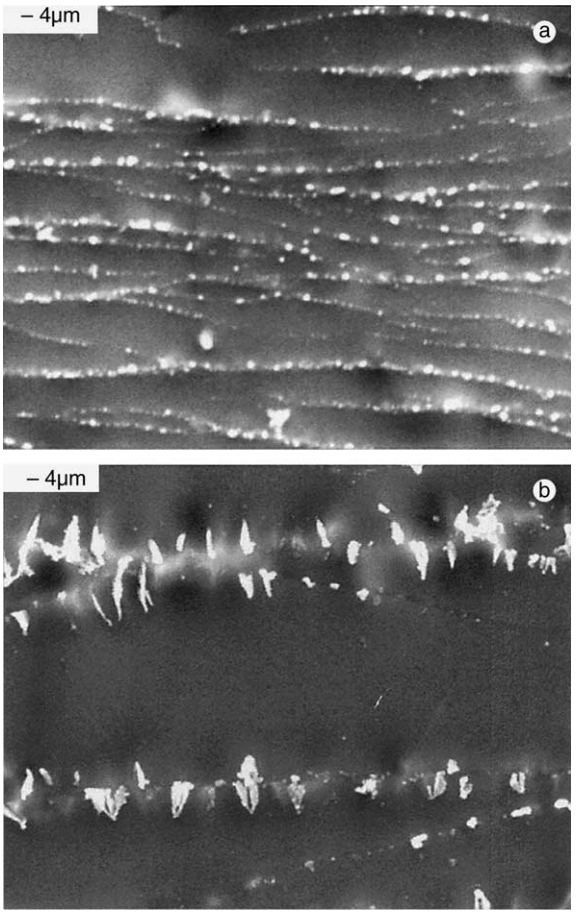

Fig. 6. SEM observations (75 mm width) of second phase precipitates after β-quenching of Zircaloy-2 specimens, 5 mm from surface: (a) trial 1 (1273 K/water at room temperature), (b) trial 5 (1323 K/water at 373 K).

Since silicon is an important impurity element in Zircaloy that favours the basket-weave structure, we have looked for the presence of silicides usually in the form of Zr_3Si using OM for specimens β-quenched at different temperatures (Table 2). We have observed silicide particles in the size range 1 to 3 μm for specimens β-quenched even at 1373 K (trial 7). This implies that the dissolution temperature for Si with a concentration level of about 100 ppm is around 1373 K; consistent with the results reported by Charquet and Alheritiere [6].

3. Analysis

The elements Cr and Fe in zirconium alloys are found in the form of second phase particles (SPP) which precipitate on $\beta \rightarrow \alpha$ transformation. In Zircaloy-2 the SPP are mainly $Zr(Cr,Fe)_2$ and $Zr_2(Ni,Fe)$, whereas Zircaloy-4 has only the former unless the Ni impurity level is high. These precipitates are based on the hcp $ZrCr_2$ Laves phase and the body-centred tetragonal Zr_2Ni Zintl phase with Fe replacing Cr and Ni in proportions depending on the alloy composition and particular heat treatment [11,12].

The decomposition and evolution of SPP in alloys usually take place by nucleation, growth and coarsening. In dilute alloys such as Zircaloy-2, we suppose that during the early stages of decomposition, nucleation and growth occur by diffusional growth of isolated and non-interacting precipitates with uniform size. At a later stage of the precipitation process, i.e. towards the end of the nucleation-growth, a spectrum of particle size distribution is established. This causes the growth of larger particles at the expense of smaller particles, which dissolve again giving rise to a change of particle size distribution. This process is referred to as coarsening or the Ostwald ripening. The coarsening is a slower process than nucleation-growth. In our evaluation here, we treat these processes separately and assume that during β-quenching of Zircaloy only nucleation and diffusional growth is operative.

3.1. Nucleation and growth of SPP

3.1.1. Theory

The alloying elements Fe and Cr in Zircaloy are in solid solution in the high temperature phase (β phase). As temperature is lowered into $\beta + \alpha$ region the alloying elements precipitate to form $Zr(Cr,Fe)_2$. Fluctuations in composition in the two phase region ($\beta + \alpha$) lower the free energy of the alloy and hence resulting the formation of stable second phase nuclei. These nuclei then grow by diffusion in the concentration gradient field of the depletion zone. This implies that the homogeneous solid solution in the $\beta + \alpha$ phase is metastable leading to nucleation and growth of second phase, sometimes generically referred to as χ phase. For the purpose of our evaluation we assume that $Zr(Cr,Fe)_2$ precipitates in Zircaloy are spherical with mean radius R.

Suppose the homogeneous solid solution is quenched not too deeply into the metastable regime of the miscibility gap. If in this region the solution is isothermally heated for a certain duration, a distribution of microclusters containing atoms of alloying elements Fe and Cr will form within grain boundaries. The formation of stable nuclei requires that a potential barrier has to be overcome (typically of the order of k_BT, k_B being the Boltzmann constant). Thermodynamic stability is reached when the supersaturation $\Delta c = c - c_\infty = 0$, where c is the solute concentration in the material and c_∞ is the terminal solubility of the solute.

The alloying elements in the matrix reach the nucleus of SPP, beyond the critical range, by diffusion. The concentration field $c(r)$ outside the spherical particle of radius R, in a steady state, is given by $c(r) = \bar{c} + (R/r)(c_R - \bar{c})$, where $\bar{c}$ is the mean concentration

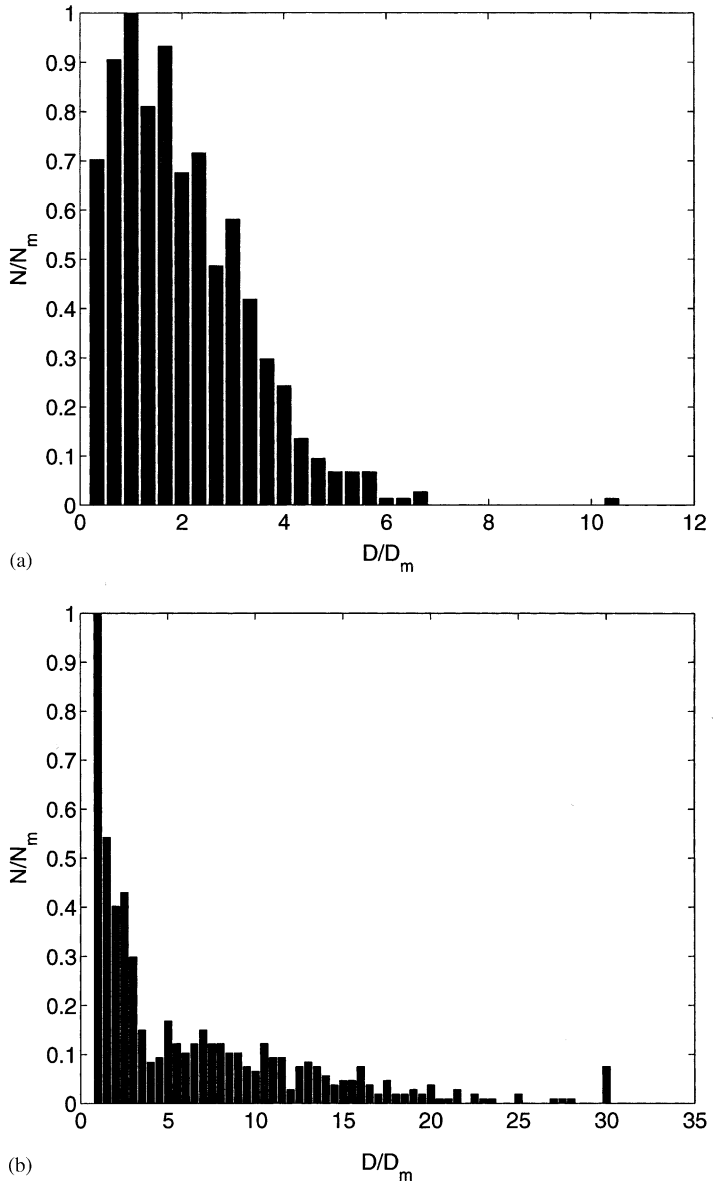

Fig. 7. Size distributions of second phase precipitates obtained by SEM after β-quenching of Zircaloy-2 specimens, 5 mm from surface, where N is the number of particles and D the particle diameter: (a) trial 1 (1273 K/water at room temperature) with $D_m = 75$ nm, $N_m = 74$, (b) trial 5 (1325 K/water at 373 K) with $D_m = 50$ nm, $N_m = 107$.

Table 3
Mean SPP size measured by SEM at radial depths 5 and 15 mm

Trial no.	Cooling rate (K s^{-1})		Mean size (μm)	
	5-mm depth	20-mm depth	5-mm depth	15-mm depth
1	58	35	0.14	0.13
5	6.6	6.3	0.31	0.30
1	(973 K h^{-1})		0.14	0.18

(Appendix A). Moreover, it can be shown that the growth rate of the particle is described by

$$\frac{dR}{dt} = Dk_s\left(1 - \frac{R_c}{R}\right)\frac{1}{R}, \tag{1}$$

where D is the solute diffusivity (Appendix A). The concentration ratio k_s and the critical radius for nucleation R_c, respectively are given by

Table 4
Values of parameters for SPP in Zircaloy [13]

Interfacial tension	$\gamma = 0.5$–$1.0\ \mathrm{J\,m^{-2}}$
Molar volume	$V_m = 9.0 \times 10^{-6}\ \mathrm{m^3\,mol^{-1}}$
Solubility limit	$c_\infty(T) = 1091.27\exp(-18515.73/\mathscr{R}T)$ ppm, $T \leqslant T_{tr}$ $c_\infty(T) = c_\infty(T_{tr}) + \frac{40}{3}(T - T_{tr})$, otherwise
Threshold temperature	$T_{tr} = 1080$ K
Molar gas constant	$\mathscr{R} = 8.3145\ \mathrm{J\,mol^{-1}\,K^{-1}}$

$$k_s = \frac{\bar{c} - c_\infty}{c_p} \quad \text{and} \quad R_c = \boldsymbol{a}\frac{c_\infty}{\bar{c} - c_\infty}, \tag{2}$$

where c_p is the composition of the precipitate, $\boldsymbol{a} = 2\gamma V_m/\mathscr{R}T$, γ is the surface tension of the precipitate, V_m is its molar volume ($c_p = 1/V_m$) and $\mathscr{R}$ is the gas constant. The values for these parameters for SPP in Zircaloy are listed in Table 4 [13]. We should note that the expression for c_∞ given in Table 4 is obtained by fitting the solubility limit vs. temperature data in the interval $873 \leqslant T \leqslant 1123$ K from a phase diagram [14].

In Eq. (1), D is the diffusion coefficient (diffusivity) for the participating alloying elements, namely Fe and Cr in Zircaloy. The relation for the temperature dependence of the diffusion coefficient is given by $D = D_0\exp(-Q/\mathscr{R}T)$ where the constants D_0 and Q are listed in Table 5 based on the work of Pande et al. [15] for lattice diffusivity, see also [16]. Pande et al. measured the diffusion coefficients of Fe and Cr in Zircaloy-2 in both α and β phases. Their data show the presence of two phase α + β region. The diffusivity in this region is most likely a weighted average of the diffusivities of each phase, amount of which varies during the transition. We have plotted the diffusivity as a function of temperature in Fig. 8(a) using the data presented in Table 5.

3.1.2. β-quenching

The mechanism for the growth of SPP is the atomic mobility (diffusivity) of substitutional solutes in the alloy toward the nucleus of the second phase and the driving force for precipitation (solubility limit). The latter being the free energy change during precipitation. For example, in Zircaloy-2 the diffusivity of chromium and iron determines the growth rate of Zr–Cr–Fe particles. In β-quenched Zircaloy-2 the particles form a chain-like network along grain boundaries, Fig. 6 (see also [17]). Hence the appropriate diffusivity for the solutes would be the grain boundary diffusivity rather than the lattice diffusivity, given in Table 5, based on the work of Pande et al. [15]. To our knowledge, there are no specific data on grain boundary diffusivity in Zircaloy-2 reported in literature. However, it is known both theoretically and experimentally that the diffusivity of substitutional solute elements in grain boundaries are substantially larger than in the matrix, especially at lower temperatures [18]. For example, the measurements of Agarwala et al. [19] show that the diffusivity of Cr in zirconium grain boundary is significantly higher than in the matrix both in α and β phase but primarily in α phase, see also [16]. The data of Agarwala et al. indicate that the ratio of the grain boundary to lattice diffusivity is $D_{gb}/D_l = 1255.66\exp(Q/\mathscr{R}T)$, with $Q = 25\,300\ \mathrm{J\,mol^{-1}}$, Fig. 8(b). Hence, based on the these observations it is justifiable to increase the diffusivities for Cr and Fe in Zircaloy in the grain boundaries relative to their diffusivity in the lattice.

Table 5
Diffusion constants for Fe and Cr in Zircaloy-2 [15]

Element	Temperature (°C)			
	650–780		980–1250	
	D_0 ($\mathrm{m^2\,s^{-1}}$)	Q ($\mathrm{J\,mol^{-1}}$)	D_0 ($\mathrm{m^2\,s^{-1}}$)	Q ($\mathrm{J\,mol^{-1}}$)
Fe	2.56×10^{-12}	103 400	1.03×10^{-6}	195 800
Cr	2.91×10^{-10}	149 000	6.31×10^{-6}	213 600

For computational convenience we have multiplied the effective diffusivity of the considered solutes by a factor of 450, i.e. we put $D_{eff} = 450D$. We use Eq. (1) to calculate the particle growth during quenching by taking the cooling process as a series of isothermal increments. Meaning that, the cooling time is divided into a number of time steps, where at each time step the temperature is kept constant with its value less than the previous time step. Particle growth at each time step is calculated and the particle size is updated. More specifically, we rewrite Eq. (1) in the form

$$\frac{du}{d\tau} = \frac{u - 1}{u^2}, \tag{3}$$

where $u = R/R_c$ and $d\tau = (D_{eff}/R_c^2)\,dt$. Eq. (3) is discretised and solved by Euler's method according to

$$u_{n+1} = u_n + h\frac{u_n - 1}{u_n^2}, \tag{4}$$

where n is an iteration index and h is a scaled time step increment:

$$h = \frac{T_q - T_f}{q_t}\frac{D_{eff}}{R_c^2}\frac{k_s}{N}. \tag{5}$$

Here T_q is the starting (quenching) temperature (in β phase), T_f is the effective final temperature, q_t is the cooling rate and N is the number of time increments.

In our computations we have selected the following values as input: $T_q = 1073$ K, $T_f = 873$ K, $N = 4000$, $u_0 = 1.01$, and the pertinent data in Tables 4 and 5 with $\gamma = 1\ \mathrm{J\,s^{-1}}$. The results of our computations are

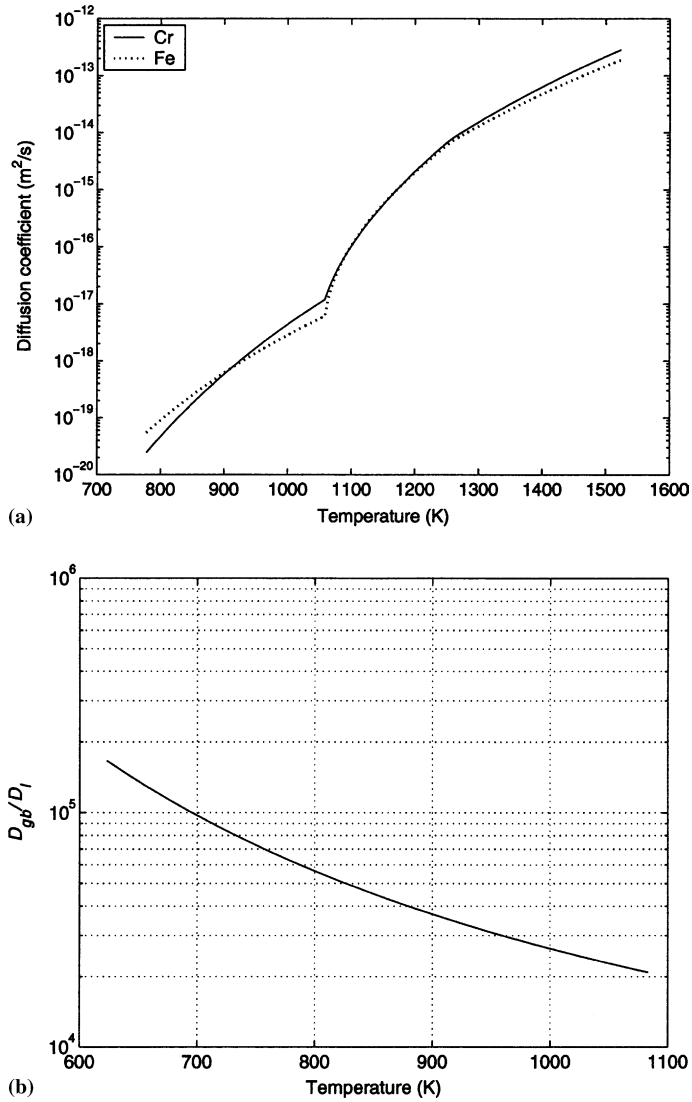

Fig. 8. (a) Diffusivity vs. temperature for Fe and Cr in Zircaloy-2 [15]. (b) The ratio of the grain boundary diffusivity to the lattice diffusivity vs. temperature for Cr in α phase of zirconium [19].

displayed in Fig. 9. It can be seen from the plots that the SPP radii stabilise to $R \approx 0.16$ and 0.05 μm for $q_t = 6$ and 60 K s^{-1}, respectively. These values are of the same order as the particle diameters listed in Table 3.

3.2. Annealing in α phase

An annealing test made on trial 1 pin (973 K h^{-1} after β-quenching) showed very little or no SPP growth, Table 3. This effect can be evaluated using a coarsening theory, which we have attempted to do in the present section.

To evaluate the annealing test (973 K h^{-1}, see Table 3), we may apply the coarsening second order kinetics of Kahlweit [20], which has been validated for SPP in Zircaloy by Gros and Wadier [13]. Kahlweit's model is based on the Lifshitz and Slyozov theory of coarsening [21]. Lifshitz and Slyozov derived the following formula in the asymptotic limit for the mean particle radius as a function of time t:

$$R^3 - R_0^3 = \frac{4}{9} D \boldsymbol{a} c_\infty t \equiv \alpha_{LS} t, \tag{6}$$

where R_0 is the initial particle radius prior to annealing, D is the solute diffusivity and other symbols were defined earlier in the text and their values are given in Table 4. Gros and Wadier [13] identified the temperature dependence of the kinetic coefficient α_{LS} and obtained the

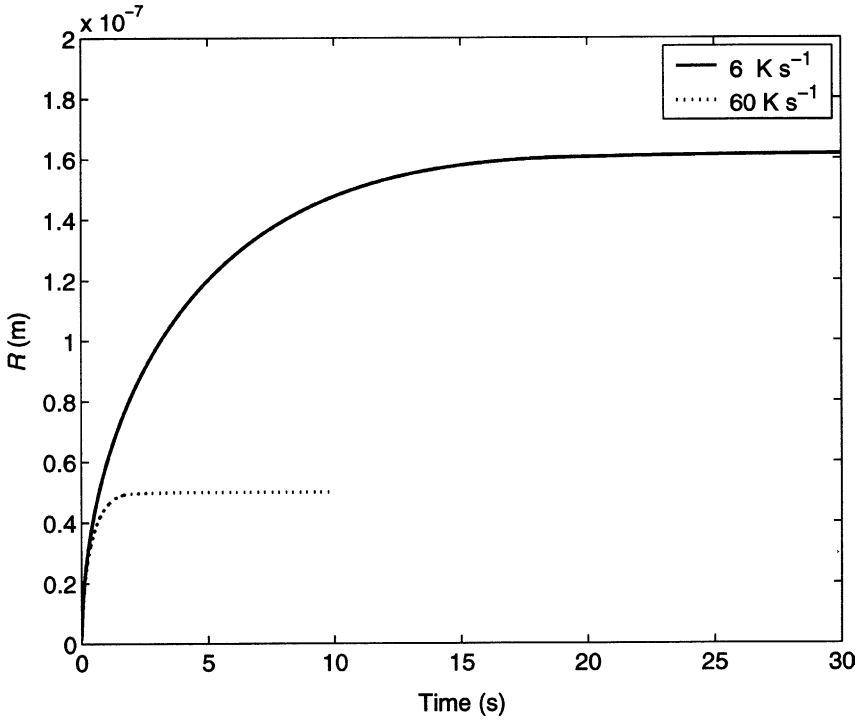

Fig. 9. Nucleation and growth of an SPP during β-quenching. Particle radius R vs. time at cooling rates $q_t = 6\ \mathrm{K\,s^{-1}}$ and $q_t = 60\ \mathrm{K\,s^{-1}}$.

following working equation for the mean particle diameter $\boldsymbol{D}$:

$$\boldsymbol{D}^3 - \boldsymbol{D}_0^3 = \frac{\mathscr{K}}{T^2}\exp\left(-\frac{Q}{\mathscr{R}T}\right)t, \tag{7}$$

with $\mathscr{K} = 1.11 \times 10^{-11}\ \mathrm{m^3\,s^{-1}\,K^2}$ and $Q/\mathscr{R} = 18\,700$ K for standard Zircaloy-4.

Let's use relation (7) to predict particle size growth in Zircaloy. We assume $\boldsymbol{D}_0 = 140$ nm (measured result) and compute $\boldsymbol{D}$ as a function of time for two temperatures $T = 973$ and 1053 K. The results are presented in Fig. 10. The computation is in agreement with the measurements reported in Table 3. It shows that after 1 h of annealing at 973 K the particle size increases from $\boldsymbol{D}_0 = 140$ nm to $\boldsymbol{D} = 143$ nm, i.e. hardly any growth that can be detected by SEM. In conclusion, the Lifshitz–Slyozov theory seems to explain the small growth of SPP observed during this annealing.

3.3. Lamella growth in α phase

The formation and growth of the α-lamella structure may be described by the kinetic theory of phase ordering. In this context we regard growth of ordered domains (here α-lamella) the size of which increases at a constant rate during cooling from the β phase. The characteristic size of the domain is considered to be the lamella thickness (or plate width).

A theory of domain growth was originally formulated by Lifshitz [22] and it is based on the argument that the driving force for domain growth is the specific energy of all the boundaries. Accordingly, the time evolution of the mean domain size L is described by the growth law:

$$L^2 - L_0^2 = 2Kt, \tag{8}$$

where $K = D\overline{E}a^2/k_B T$, $\overline{E}$ is the surface energy density for α-domain, a is the atomic distance, k_B is the Boltzmann constant, L_0 is the initial domain diameter, and D is some diffusivity.

Using Eq. (8) we now attempt to fit the experimental data, presented in Fig. 4, to this equation in order to identify the parameters for this kind of cooling in Zircaloy. Let us rewrite (8) in the form

$$L = \sqrt{L_0^2 + 2K\Delta T q_t^{-1}}, \tag{9}$$

where ΔT is the temperature interval over which the cooling rate is measured. We select the data measured only at lateral depth of 5 mm. The result of our exercise is depicted in Fig. 11, where we used $L_0 = 0.1$ μm and $C_0 = 2K\Delta T = 135.246\ \mu\mathrm{m^2\,K\,s^{-1}}$. As can be seen the fit is quite satisfactory bearing in mind the scatter in the measurements.

It would be worthy to make predictions of lamella width vs. time directly by using Eq. (8) or the corresponding differential equation, $\mathrm{d}L/\mathrm{d}t = K/L$, provided

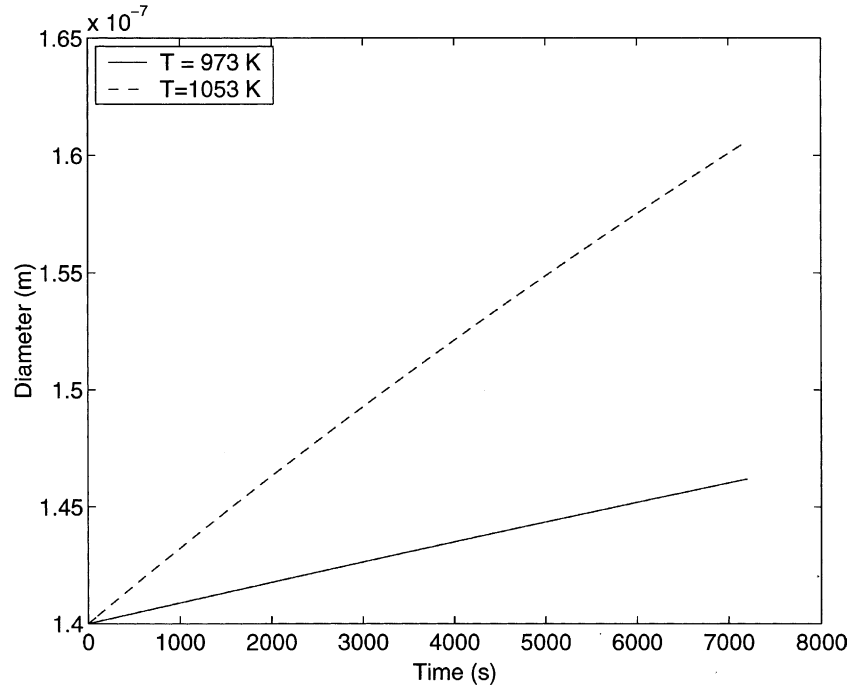

Fig. 10. Particle diameter vs. time using the Lifshitz–Slyozov law expressed by Eq. (7) with $D_0 = 140$ nm.

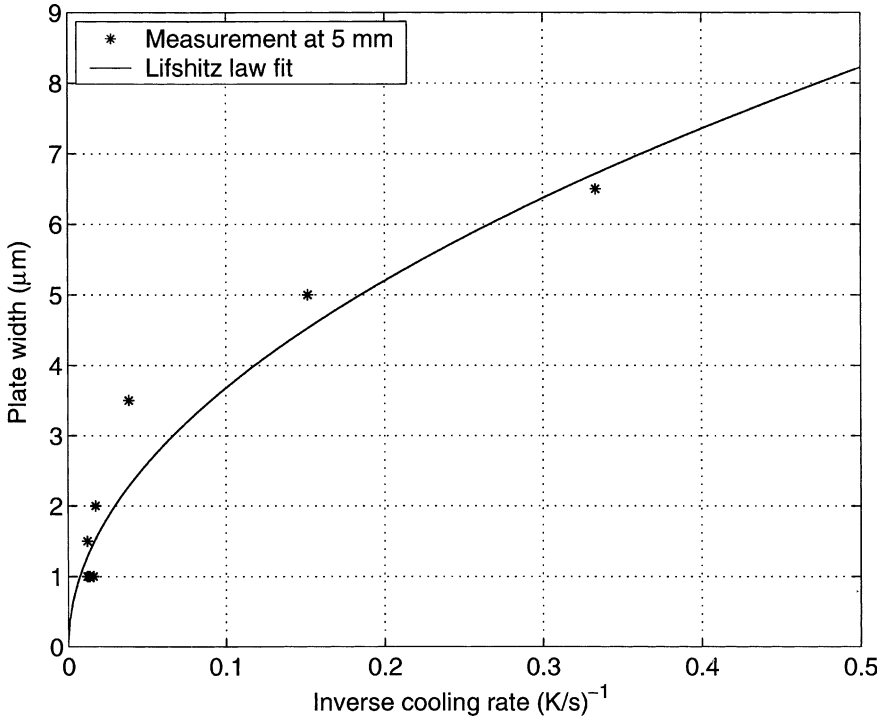

Fig. 11. Data on α-lamella width measured by OM at a lateral depth of 5 mm for β-quenched specimens that were subjected to different cooling rates and the fit according to Eq. (9).

the temperature dependence of the diffusivity and the value of the surface energy density are known for Zircaloy. This pursuit, however, is attempted elsewhere [23].

3.4. Grain growth in β phase

The basket-weave structure in α phase appears as relatively short plates that grow from copious nucleation sites in the prior β phase. The plates in the basket-weave structure intersect each other within the prior β phase grains. On the other hand, the parallel-plate structure is made-up of long plates that form and grow from the prior β-grain boundaries [24]. It is known that large prior β-grain size promotes parallel-plate structure, whereas small prior β-grain size favours basket-weave structure. Also impurities in metals hamper grain growth [25]. Hence, the study of the β phase grain growth is important for characterising the microstructure morphology of the α phase.

Most of the normal grain growth theories for isothermal annealing predict a time law of the form [26]

$$\overline{G} = kt^n, \tag{10}$$

where $\overline{G}$ is the mean grain size, n is a constant and k is another constant which exhibits Arrhenius temperature dependence. Furthermore, there are scatter in experimental values for n, with a maximum value of 0.5 and a mean value in the vicinity of 0.4 for polycrystalline metals [27].

We have made a least squares fit to the mean prior β-grain size data depicted in Fig. 5. In the evaluated temperature interval we find the following relation according to Eq. (10):

$$\overline{G} = 37.8t^{0.435}. \tag{11}$$

Here $\overline{G}$ measures in microns and t in seconds, see Fig. 12.

Despite its importance there is a paucity of experimental data on Zircaloy β-grain size and its time/temperature dependence in open literature. We are only aware of the work of Holt [7] and Fong and Northwood [25] on Zircaloy-4 samples, containing different levels of impurities. Fong and Northwood determined the mean prior β-grain size of specimens after simulated heat treatment and β-quenching in water by OM using four test-lines intersecting at 45° with intercepts perpendicular to the test-lines. For example, for the their sample B with a similar impurity level as ours, namely (Si, C, P) = (89, 150, <50) ppm, at $T = 1323$ K, our fitting exercise gives $\overline{G} = 78.4t^{0.19}$. Holt's data, although less certain [8] than the latter work, are in the same order as predicted by this relation. This means that their Zircaloy-4 specimens exhibit much less β phase grain growth than we

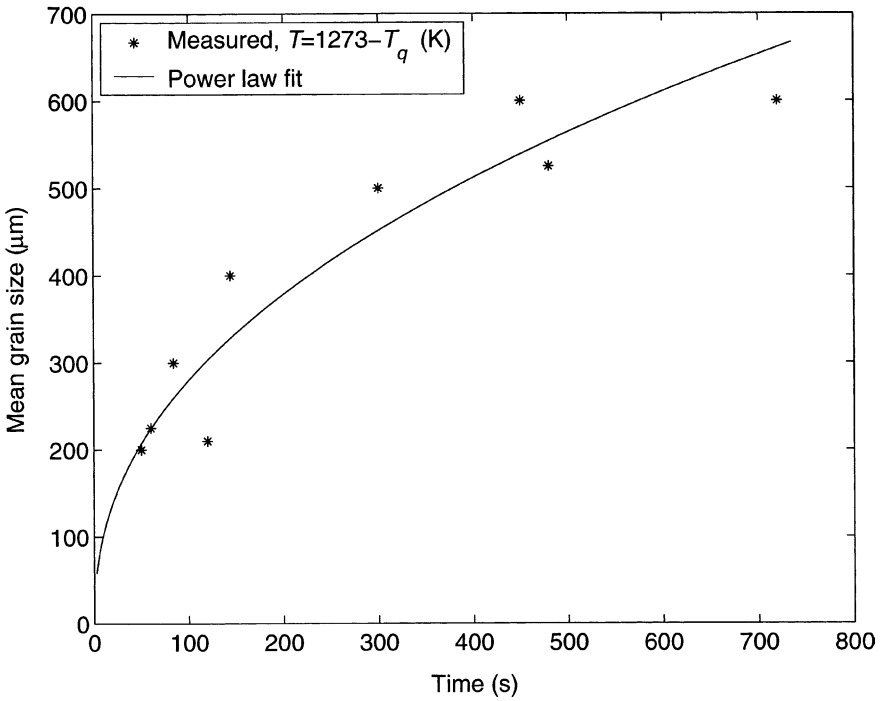

Fig. 12. Prior β phase grain size for Zircaloy-2 vs. hold-time in β phase ($\Delta T = T_q - 1273$ K) and the fit according to Eq. (11).

predict for low-tin Zircaloy-2 with Eq. (11), provided everything else is equal.

4. Conclusion

The effect of β-quenching rate on the microstructure of low-tin Zircaloy-2 has been studied using OM and SEM. In the employed cooling rates, ranging from 3 to 83 $\mathrm{K\,s^{-1}}$, all the tested specimens indicated the Widmanstätten α phase basket-weave structures. We have attempted to show that physically-based models can be used to explain certain important microstructural observations made for Zircaloy subjected to β-quenching.

We classified the decomposition and evolution of SPP during $\beta \rightarrow \alpha$ transformation to nucleation, growth and coarsening stages. We used classical homogeneous nucleation and growth kinetic theory to calculate the mean SPP size under cooling conditions. In particular, we simulated the tests, one with low cooling rate, the other with relatively high cooling rate to retrodict the mean SPP size. Our selected models only contain measurable parameters such as the diffusivity, the surface energy, the terminal solubility, etc., which we have taken from the literature. We found that the theory satisfactorily estimate the particle size obtained after quenching. Also employing the coarsening theory of Lifshitz and Slyozov we could retrodict the mean particle size measured after the annealing test (973 $\mathrm{K\,h^{-1}}$) on one of the quenched specimens.

In Section 3.3 we analysed the Widmanstätten structures of Zircaloy obtained on $\beta \rightarrow \alpha$ cooling. We applied Lifshitz's growth law to model the experimental data on a plate width vs. cooling rate. The outcome is satisfactory. The physical constants appearing in Lifshitz's theory (diffusion coefficient, surface energy, etc.) were, however, fitted to the data. Subsequently, we analysed grain growth during annealing in β phase prior to quenching. Although the measured average prior β-grain size data fit well against general theoretical predictions, a large scatter in the data suggests that prudence needs to be exercised to draw any definite conclusion on these results. More careful experimental data on β-grain growth and grain size distribution are needed for a more explicit resolution. Also, for a more detailed analysis of SPP, additional microscopy measurements including transmission electron microscopy are desirable. As a final remark, the role of all the existing impurities in Zircaloy on the microstructure has not yet been properly systematised. Research in that direction is valuable. Microstructure and composition govern the alloy's performance (corrosion, creep, strength, etc.) during service, which can be optimised and controlled through improved fabrication.

Appendix A. Equations for particle nucleation and growth

The equations used in our analysis for nucleation and growth of second phase precipitates are derived in this section. The minimum energy required to form a nucleus of radius R from a metastable solid solution is expressed by

$$\mathscr{F}_{\min} = S_d\left(\gamma R^{d-1} - \frac{1}{d}\mu_{\mathrm{eff}} R^d\right), \tag{A.1}$$

where d is the dimension of the system, $S_3 = 4\pi$, $S_2 = 2\pi$, γ is the interfacial surface tension and μ_{eff} is the chemical potential difference per unit volume between the metastable and stable phases. $\mathscr{F}_{\min}$ can be considered as a potential barrier for the formation of stable nucleus. It has a maximum when $R = R_{\mathrm{c}}$, where

$$R_{\mathrm{c}} = \frac{\gamma(d-1)}{\mu_{\mathrm{eff}}}. \tag{A.2}$$

From chemical thermodynamics the change in chemical potential is related to the concentrations according to

$$\mu_{\mathrm{eff}} = \frac{\mathscr{R}T}{V_{\mathrm{m}}} \ln\left(\frac{c}{c_\infty}\right), \tag{A.3}$$

where V_{m} is the molar volume of the precipitate, $\mathscr{R}$ is the gas constant, T is the temperature, c is the solute concentration in the matrix and c_∞ is the terminal solubility of the solute. The saturation concentration above the surface of the particle of radius R can be calculated by combining Eqs. (A.2) and (A.3), which yields

$$c_R = c_\infty \mathrm{e}^{\boldsymbol{a}/R} \approx c_\infty\left(1 + \frac{\boldsymbol{a}}{R}\right), \tag{A.4}$$

where c_R is the composition of matrix at the matrix/particle interface and $\boldsymbol{a} = \gamma(d-1)V_{\mathrm{m}}/\mathscr{R}T$. Eq. (A.4) is the well-known Gibbs–Thomson relation.

Because the concentration of substitutional elements in Zircaloy is relatively small, the concentration around a particle of radius R can be regarded as equal, at each instant, to the steady state distribution $c(r)$ which obeys the Laplace equation

$$\nabla^2 c(r) = 0, \tag{A.5}$$

with boundary condition

$$c(R) = c_R \quad \text{and}_{r\rightarrow\infty} c(r) = \bar{c}. \tag{A.6}$$

The unique solution of Eq. (A.5), for the spherically symmetric concentration, satisfying Eq. (A.6) is

$$c(r) = \bar{c} + \frac{R}{r}(c_R - \bar{c}). \tag{A.7}$$

The diffusive flux at a particle surface is equal to the rate of change of the particle radius according to

$$\frac{dR}{dt} = \left(\frac{D}{c_p - c_R}\right)\left.\frac{\partial c}{\partial r}\right|_{r=R}, \tag{A.8}$$

where D is the solute diffusivity and c_p is the composition of the precipitate. Hence, the diffusive flux with Eq. (A.8) gives

$$\frac{dR}{dt} = \frac{D}{R}\frac{\bar{c} - c_R}{c_p - c_R}. \tag{A.9}$$

The steady-state ansatz (A.5) used for the kinetics of particle growth, where one sets $\partial c/\partial t = 0$, is sometimes referred to as the invariant field approximation. It offers an accurate description of growth if $(\bar{c} - c_R)/(c_p - \bar{c}) \ll 1$, [28].

Using Eqs. (A.2)–(A.4) we can write Eq. (A.9) in terms of the critical radius at the onset of nucleation R_c and the critical concentration (solubility limit) c_∞, viz.

$$\frac{dR}{dt} = D\left(\frac{\bar{c} - c_\infty}{c_p}\right)\left(1 - \frac{R_c}{R}\right)\frac{1}{R}, \tag{A.10}$$

where we assumed $c_p \gg c_R$. This is the same as Eq. (1) in Section 3.1, where we introduced $k_s = (\bar{c} - c_\infty)/c_p$.

References

[1] M. Corchia, F. Righini, J. Nucl. Mater. 97 (1981) 137.
[2] C. Lemaignan, A.T. Motta, in: R.W. Cahn, P. Haasen, E.J. Kramer (Eds.), Nuclear Materials, Material Science and Technology, vol. 10B, VCH, Weinheim, 1994, Chapter 7.
[3] G. Östberg, Jernkont. Ann. 145 (1961) 119.
[4] G. Ökvist, K. Källström, J. Nucl. Mater. 35 (1970) 316.
[5] W.L. Fong, D.O. Northwood, Metallography 15 (1982) 27.
[6] D. Charquet, E. Alheritiere, in: R. Adamson, L. van Swam (Eds.), Seventh International Symposium: Zirconium in Nuclear Industry, ASTM STP 939, ASTM, Philadelphia, 1987, p. 284.
[7] R.A. Holt, J. Nucl. Mater. 35 (1970) 322.
[8] R.A. Holt, J. Nucl. Mater. 47 (1970) 262.
[9] O.T. Woo, K. Tangri, J. Nucl. Mater. 79 (1979) 82.
[10] Annual Book of ASTM Standards, Section 2, Nonferrous Metal Products: B 811–97, American Society for Testing and Materials, West Conshohocken, PA, 2000.
[11] P. Chemelle, D.B. Knorr, J.B. van der Sande, R. Pelloux, J. Nucl. Mater. 113 (1983) 58.
[12] X.Y. Meng, D.O. Northwood, J. Nucl. Mater. 168 (1989) 125.
[13] J.F. Gros, J.F. Wadier, J. Nucl. Mater. 172 (1990) 85.
[14] D. Charquet, R. Hahn, E. Ortlieb, J.P. Gros, J.P. Wadier, in: L. van Swam, C. Euken (Eds.), Seventh International Symposium: Zirconium in Nuclear Industry, ASTM STP 1023, ASTM, Philadelphia, 1988, p. 405.
[15] B.M. Pande, M.C. Naik, R. Agarwala, J. Nucl. Mater. 28 (1968) 324.
[16] D.L. Douglass, The Metallurgy of Zirconium, IAEA, Vienna, 1971.
[17] R. Kuwae, K. Sato, E. Higashinakagawa, J. Kawashima, S. Nakamura, J. Nucl. Mater. 119 (1983) 229.
[18] G.R. Purdy, in: R.W. Cahn, P. Haasen, E.J. Kramer (Eds.), Phase Transformation in Materials, Material Science and Technology, VCH, Weinheim, 1991, Chapter 5.
[19] R.P. Agarwala, S.P. Murarka, M.S. Anand, Trans. AIME 233 (1965) 986.
[20] M. Kahlweit, Adv. Colloid Interf. Sci. 5 (1975) 1.
[21] I.M. Lifshitz, V.V. Slyozov, J. Phys. Chem. Solids 19 (1961) 35.
[22] I.M. Lifshitz, Sov. Phys. JETP 15 (1962) 939.
[23] A.R. Massih, L.O. Jernkvist, Phase ordering under quenching: a case of zirconium alloys, Quantum Technologies report PM 03-004, 2003, Uppsala. To be published.
[24] V. Quach, D.O. Northwood, Metallography 17 (1984) 191.
[25] W.L. Fong, D.O. Northwood, Microstruct. Sci. 10 (1982) 123.
[26] H.V. Atkinson, Acta Metall. 36 (1988) 469.
[27] M.P. Anderson, D.J. Srolovitz, G.S. Grest, P.S. Sahni, in: Materials Society Symposium Proceeding, vol. 22, Elsevier Science, Amsterdam, 1984, p. 457.
[28] H.B. Aaron, D. Fainstein, G.R. Kotler, J. Appl. Phys. 41 (1970) 4404.